Robustness of conventional and topologically protected edge states in phononic crystal plates

Yabin Jin,[1,2,*] Daniel Torrent,[3,†] and Bahram Djafari-Rouhani[4]

[1]*School of Aerospace Engineering and Applied Mechanics and Institute for Advanced Study, Tongji University, 200092 Shanghai, China*

[2]*Institut de Mécanique et d'Ingénierie, UMR CNRS 5295, Université de Bordeaux, 33405 Talence, France*

[3]*GROC-UJI, Institut de Noves Tecnologies de la Imatge, Universitat Jaume I, 12071, Castello, Spain*

[4]*Institut d'Electronique, de Microélectonique et de Nanotechnologie, UMR CNRS 8520, Département de Physique, Université de Lille, 59650 Villeneuve d'Ascq, France*

(Received 9 February 2018; revised manuscript received 16 June 2018; published 29 August 2018)

Many efforts have been devoted to studying the robustness of topologically protected edge states in acoustics; however, the robustness of conventional edge states is rarely reported. In this work we theoretically study interface acoustic states appearing in finite arrays of resonators on a thin plate with topologically protected and conventional designs. Topologically protected interface states are first analyzed by employing the concept of breaking inversion symmetry within the unit cell of a honeycomb lattice for cylindrical and spherical resonators; we further demonstrate the robustness of the wave propagation along a zigzag path containing sharp corners and defects. In parallel, a conventional interface state is also designed and compared to the same situations. We found that the conventional interface state suffers backscattering in the zigzag path while it can show a more confined wave transport in some cases. The presence of a defect along the propagation path scatters the conventional interface wave and in particular can prohibit full propagation in the presence of a localized state at the defect. Then, we show that the immunity of the topologically protected design needs the interface to be surrounded by at least two hexagons of the phononic crystals on both sides, especially at the sharp corners in the zigzag path, while the conventional design only needs one hexagon of bulk media with the advantage of compact wave transport. Position and height disorders are further introduced to the interface pillars for both designs. It is revealed that in both designs, the transmission decreases quasilinearly with position disorder while it exhibits an abrupt drop with height disorder showing a transition threshold. With high disorder perturbation, waves can hardly enter the interface for the topologically protected design, while waves are trapped at the interface for the conventional design. A certain robustness against disorder is exhibited for conventional edge states. This work provides insight into the interface states in micro- and nanoscale characterization and figures out the behaviors for both topologically protected and conventional interface states.

DOI: 10.1103/PhysRevB.98.054307

I. INTRODUCTION

Phononic crystal plates [1–3], which consist of periodic resonators or scatters such as pillars attached to an elastic plate, have received increasing attention from the past decade. These structures can exhibit hybridization and Bragg band gaps simultaneously, so that they present aspects of both phononic crystals [4–8] and acoustic metamaterials [9–12]. In the particular case of flexural motion in a pillared plate, an analytical model has been introduced to consider the pillar as a pointlike resonator attached to the plate by a string and displaying out-of-plane motion. This model has recently demonstrated the possibility of topologically protected edge states [13,14]. When the resonators are organized in a honeycomb arrangement, the dispersion curves of flexural waves present the so-called Dirac points, and bounded edge states can be found for finite slabs [15]. Then, by breaking inversion symmetry in the unit cell of the honeycomb arrangement, topologically nontrivial band gaps are found which support topologically protected edge states [13,16–18]. It should be noted that topological structures with realistic spheres have not been studied very much and only a few works deal with realistic pillars [16,17]. How topologically protected edge states behave with different resonators requires more study. Additionally, these realistic structures have (several) dispersion curves besides those at the Dirac point and here we show that the topological effect for flexural waves can be preserved despite these other dispersion curves.

Topologically protected edge states were originally found in electronic systems [19], and their mechanical analogs have been widely studied, like the analog to the quantum Hall effect [20], the quantum spin Hall effect [21–23], and the quantum valley Hall effect [24]. All these guided states are protected against local defects and sharp bends, which means that waves excited along one direction are free of being backscattered by disorder or defects. Edge states, however, are not unique among topological insulators, since whenever there is an interface, there is the possibility of finding guided states at this interface, and a comparison between topologically protected states and "conventional" edge states has not been reported so far for mechanical waves.

In this work, we will study topologically protected edge states in a thin elastic plate with cylindrical or spherical

*083623jinyabin@tongji.edu.cn

†dtorrent@uji.es

resonators attached to it (with a tangent contact point for spherical resonators). We will design a plate supporting both topologically protected and conventional edges states, and we will analyze their robustness for propagation along a zigzag path and under the presence of defects in the zigzag edge. Also, we will analyze the necessary size of the bulk material surrounding the interface to preserve them, supporting this type of state. An empirical way to study the disorder effect is introduced for pillars in the straight interface and the robustness of the interface states and their propagation against disorder is discussed. The paper is organized as follows: Section II will analyze the dispersion curves of the plates with attached spherical and cylindrical resonators and the existence of Dirac cones in a honeycomb lattice. In Sec. III we will design topologically protected edge states by employing two resonators with different heights or radius in the unit cell, in order to break the inversion symmetry and open a gap at the Dirac point. We build topologically protected edge states by creating a suitable interface between two of such crystals and we analyze their robustness against the presence of a defect such as a zigzag or a missing atom. We will also analyze the necessary minimum size of the bulk media surrounding the interface to preserve the existence of the edge state. Position and height disorders are introduced for pillars along a straight interface and the transmission is calculated as a measure of the capability of the edge state to transport wave in presence of disorder. In Sec. IV we will design a similar plate supporting conventional edge states and we will compare its properties with those of the topologically protected edge state. Finally, the work is summarized in Sec. V.

II. SPHERICAL AND CYLINDRICAL RESONATORS OVER A THIN ELASTIC PLATE

We consider a honeycomb arrangement of resonators [Fig. 1(a)] attached to a thin elastic plate. Two types of resonators are considered in this work: a cylindrical pillar deposited over the plate [Fig. 1(b)] and a spherical scatter attached to the plate by means of a tangent contact [Fig. 1(c)]. These two types of resonators are the most feasible from the practical point of view, especially at the micro- or nanoscale (from hundreds of nanometers to hundreds of micrometers), compared to other approaches based on inclusions in the plate.

In the numerical simulations performed in this work by means of the finite element method (FEM), the spherical and cylindrical resonators are defined as fused silica [25], with elastic modulus $E_s = E_c = 62\,\text{GPa}$, Poisson's ratio $\nu_s = \nu_c = 0.24$, and mass density $\rho_s = \rho_c = 2200\,\text{kg m}^{-3}$ where the subscripts s and c stand for sphere and cylinder, respectively. The thin plate is made of aluminum, whose elastic parameters are $E_p = 73\,\text{GPa}$, $\nu_p = 0.17$, and $\rho_p = 2730\,\text{kg m}^{-3}$, where the subscript p stands for plate. It is also useful to define the normalized frequency Ωa as

$$\Omega^2 = \omega^2 \rho_p a^2 e / D, \tag{1}$$

where $D = E_p e^3/12(1-\nu_p^2)$ is the plate's bending stiffness, a is the lattice constant (distance between the nearest two A-A or B-B points), and e is the thickness of the plate.

Figure 2(a) shows the band structure computed by the FEM of a honeycomb lattice of cylindrical resonators attached to the elastic plate ("pillared" phononic crystal plate). The radius of the cylinders is $R_c = 0.1a$ and their height $h_c = 1.2a$. The right panel shows the same lattice but with spherical resonators ("sphered" phononic crystal plate), where the spheres have the same volume as the cylinders, which results in a radius $R_s = 0.208a$. In both cases the plate's thickness is chosen as $e = 0.1a$. It is found that for $\Omega a < 5$ the antisymmetric Lamb mode, identified by its parabolic trend in the low frequency limit, interacts with the local resonant modes of the scatters [bending resonance of the cylinder as the $B1$ mode in Fig. 2(a), bending resonance of the sphere as the $B1$ mode in Fig. 2(b)]; then hybridization band gaps appear as well as nearly flat branches.

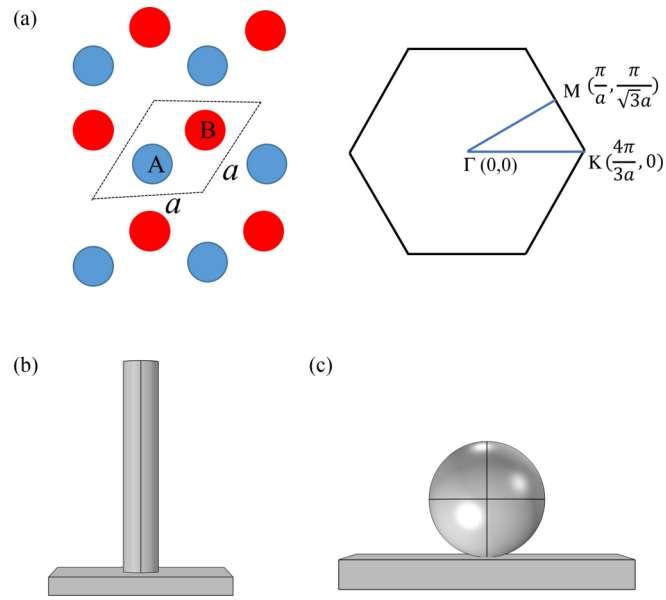

FIG. 1. (a) Phononic crystal plate with honeycomb lattice and the corresponding Brillouin zone; cylinder (b) and sphere (c) resonators are deposited on a thin plate.

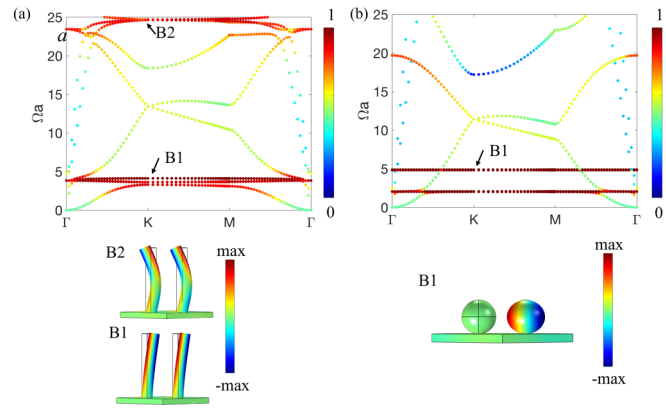

FIG. 2. Dispersion of pillared (a) and sphered (b) phononic crystal plate with honeycomb lattice arrangement with identical scatters A and B. Geometric parameters are lattice parameter a, thickness of the plate $e = 0.1a$, radius of the pillar $r_p = 0.1a$, height of the pillar $h = 1.2a$, and radius of the sphere $r_s = 0.208a$. The pillar and the sphere have the same volume. The real parts of out-of-plane displacement u_z are shown at the bottom for points $B1$ and $B2$ modes.

The degeneracy created by the existence of two resonators per unit cell results in the emergence of the so-called Dirac cone at the K point of the dispersion curves, as can be seen in Figs. 2(a) and 2(b) for cylindrical and spherical resonators, respectively. The color bar in the dispersion indicates a degree of confinement of the mode in the resonators by making a ratio α between the average displacement in the resonators and in the whole unit cell shown in Fig. 1, as [26]

$$\alpha = \frac{\iiint_{\text{resonators}} \sqrt{u_x^2 + u_y^2 + u_z^2}\, dV}{\iiint_{\text{unit cell}} \sqrt{u_x^2 + u_y^2 + u_z^2}\, dV}, \tag{2}$$

where u_x, u_y, u_z are the three displacement components in the solid, and dV is a volume element.

The existence of Dirac cones in these lattices have been widely studied in photonics [27,28] and acoustics [29,30], with remarkable properties for the propagation of waves in the vicinity of the vertex of the cones. Special mention deserves the recent rise of the domain of topological insulators [19], where topologically protected edge states with one-way propagating properties can be properly tailored on the basis of these states [13,16]. However, for elastic plates these states have been found in idealized systems of pointlike resonators [13,14], whose physical implementation has been scarcely discussed in the literature. Although other complex systems have been implemented at the macroscale [16], their realization in the micro- or nanoscale has not been properly studied yet. Therefore, the existence of Dirac cones in the structures proposed before, more suitable for the micro- or nanoscale, opens the door to an alternative type of device based on the extraordinary properties of topological insulators.

We note that the diameter and the height of the cylindrical resonator are chosen to well isolate the Dirac point from other resonant flat bands at the K point. From Fig. 2(a), the Dirac point locates more or less at the middle of the first (about $\Omega a = 5$) and the second (about $\Omega a = 25$) bending modes of the cylindrical resonators, so that these modes do not interact with the topological modes of interest.

III. TOPOLOGICALLY PROTECTED INTERFACE STATES

In the honeycomb lattice the mirror symmetry is broken when the two resonators A and B of the unit cell are different. In the dispersion curves depicted in Fig. 3 the mass of resonator A is three times that of resonator B, $m_A = 3m_B$, in other words, $h_A = 3h_B$ in the cylindrical pillar and $r_A = 3^{1/3} r_B$ in the spherical case. It is clear that a band gap for the flexural mode is opened at the Dirac cone for both cylindrical and spherical resonators shown in Fig. 3. It is well known that the Chern number for the upper and lower bands with respect to the gap have opposite signs, what makes these systems suitable to support topologically protected states in this nontrivial band gap [13,16], resulting from the elastic analog of quantum valley Hall effect. Although this nontrivial band gap is only for flexural waves, it is possible to choose the parameters of the crystals such that the flexural wave remains almost independent from symmetric and shear-horizontal waves [31], and the topologically protected states for flexural wave works [16,17].

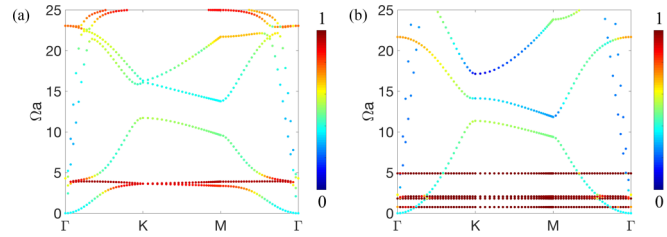

FIG. 3. Dispersion of pillared (a) and sphered (b) phononic crystal plate with honeycomb lattice arrangement with asymmetric resonators A and B. Geometric parameters are lattice parameter a, thickness of the plate $e = 0.1a$, radius of the pillar $r_p = 0.1a$, height of the pillar $h_A = 1.2a$, and $h_B = 0.4a$, and radius of the sphere $r_{sA} = 0.208a$ and $r_{sB} = 0.144a$. The color bar in the dispersion indicates a displacement ratio α in Eq. (2).

Figure 4 shows the geometry considered for the analysis of these states, where a stripe consisting of two lattices, B-A and A-B, is considered. The two "A" heavy resonators at the interface (marked by the black dotted rectangle at the bottom of the figure) are chosen since the band in the gap associates with the localized modes spanning between the K and K' valleys in the acoustic band; in contrast, in the case of the A-B-B-A interface, the band associates with the localized modes spanning the two valleys in the optical band [13]. As before, cylindrical [Fig. 4(a)] and spherical [Fig. 4(b)] scatters are considered. The stripe is assumed to be periodic in the x direction. From the dispersion diagram, we find an edge mode traversing the opened band gap, which is highlighted in bright color and limited by the dotted rectangle domains. The color bar in the dispersion curves indicates the degree of localization in the resonators at the interface as compared to the resonators in the whole stripe by defining the ratio β as [26]

$$\beta = \frac{\iiint_{\Lambda} \sqrt{u_x^2 + u_y^2 + u_z^2}\, dV}{\iiint_{\text{stripe}} \sqrt{u_x^2 + u_y^2 + u_z^2}\, dV}. \tag{3}$$

The nontrivial gap for the cylindrical resonator occupies the normalized frequency domain (11.5, 12.8), three times wider than that of the spherical one (11.0, 11.5) and results in a higher β value in a wider band gap as shown in the left panel of Fig. 4.

To demonstrate the topological robustness of this edge state, we construct a zigzag channel for the B-A-A-B type interface on a circular thin plate as seen in Fig. 5(a). An antisymmetric Lamb (A_0) wave source [finite white segment in Fig. 5(a)] is excited at the bottom exit of the zigzag path by applying an out-of-plane force. The two lattices of phononic crystals are separated by the zigzag interface path (limited by the red lines). A perfect matched layer (PML) is applied to surround the phononic crystals to avoid wave reflection from the boundaries. Simulations are performed in the frequency domain with time-harmonic condition. A topologically protected waveguide is able to suppress backscattering and robust transport of phonons along the zigzag interface, which are clearly demonstrated for cylindered [Fig. 5(b)] and sphered [Fig. 5(c)] resonators. The color bars shown here in the fields are the amplitude of displacement u_z, which is dominant for A_0 Lamb waves. As explained in Fig. 4, the cylindered resonator system has a wider nontrivial band gap so that the phonon transport is more

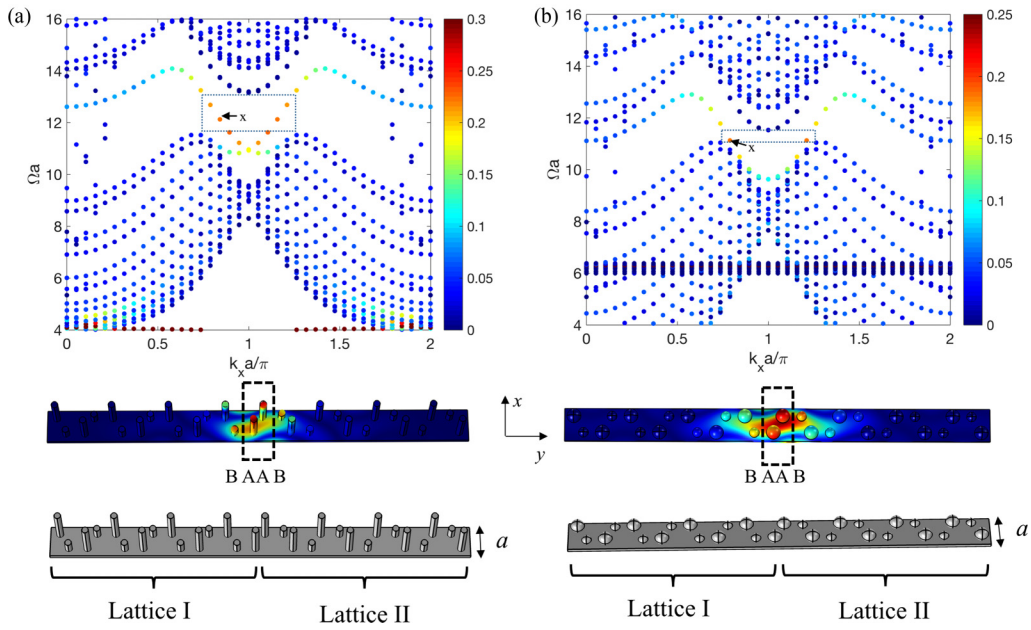

FIG. 4. Dispersion of a stripe consisting of the juxtaposition of B-A (lattice I) and A-B (lattice II) honeycomb lattices with the interface as B-A-A-B for pillared (a) and spherical (b) resonators (the geometries of the two lattices stripes are shown at the bottom). The color in the dispersion represents the ratio of total displacement localized in the A-A resonators (black dotted rectangle) over the whole stripe. The total displacement distributions at marked the "x" point in the dispersion are shown below the dispersion curves. Here the wave number $k_x a/\pi$ in dispersion is used as the stripe and is finite in the y axis but infinite in the x axis, not relating to the Brillouin zone in Fig. 1.

concentrated at the interface, with less leakage in the bulk. In Fig. 6, we remove a resonator at the middle interface as a dotted circle indicated by the red arrow in the zoomed-in insets; the same interface transports are found for both cylindered and sphered resonators, behaving as robust wave propagation after the imperfection.

Due to the smaller band gap in the case of spherical resonators, and hence less confinement of the interface mode, we limit the following discussions to the case of cylindrical pillars.

The topologically protected interface mode relies on the emergence of the nontrivial band gap from the bulk phononic crystal, which obviously requires the size of the bulk media to be sufficiently large. In the previous examples, the length of the bulk material was at least four hexagon unit cells on each side of the zigzag interface. Figure 7 shows the same simulations when the bulk media are reduced to only one hexagon on each side of the vertical straight parts of the interfaces [panel (a)] and then to one hexagon on any side of the zigzag interface [panel (b)]. Panel (a) shows that, with the minimized bulk phononic crystal, the effect of the leaky wave is strengthened and the propagating state in the upper straight interface part decreases. Nevertheless, the zigzag interface state is still visible. However, when the bulk media are further minimized as shown in panel (b), flexural waves are transported along the lower straight interface part and exit to the background plate directly, so that

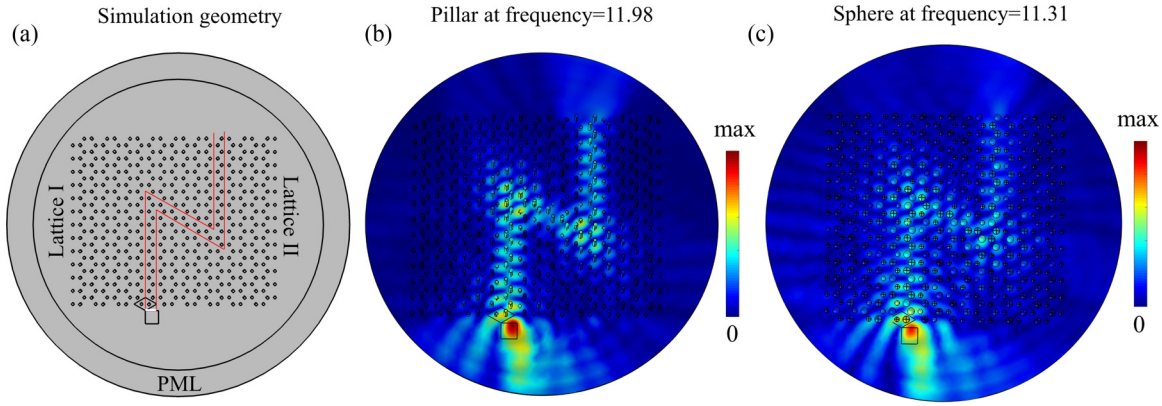

FIG. 5. (a) Schematic view of the numerical model: The phononic crystal plates consist of two lattices (as in Fig. 4) with a zigzag interface path (limited by the red lines); a finite antisymmetric Lamb wave source is excited along the white line segment (at the bottom exit of the zigzag path); a perfect marched layer (PML) is applied to surround the phononic crystal plates to avoid any wave reflection. The topologically protected edge state is excited by an antisymmetric Lamb wave at $\Omega a = 11.98$ for the pillar resonator (b) and at $\Omega a = 11.31$ for the sphere resonator (c) with a backscattering-immune property. The color bars show the amplitude of the displacement u_z.

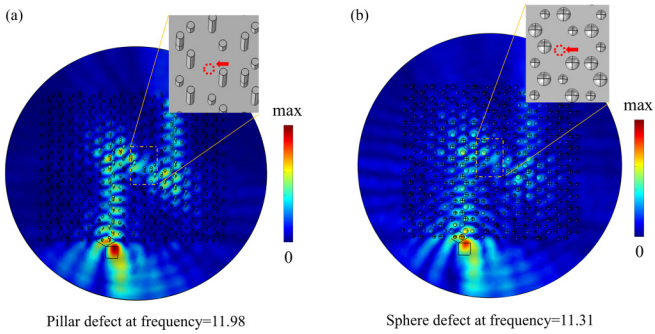

FIG. 6. The topologically protected edge state is excited at $\Omega a = 11.98$ for the pillar scatter (left panel) and at $\Omega a = 11.31$ for the sphere scatter (a) when one resonator (b) is removed (see the arrowed dotted circle in the zoomed-in inserts). The color bars show the amplitude of the displacement u_z.

the flexural vibrations do not enter the middle and the upper parts of the zigzag interface. Therefore, one hexagon of bulk media can be the minimum size for the straight interface state and at least two hexagons of bulk media are needed for the zigzag interface, especially around the sharp corners.

In previous studies [18,21,22], most works have reported that the topologically protected edge state can support local disorder in the edge path. However, up to now, the influence of the disorder has been mainly limited to a small part of the path and disorder along the whole edge path is rarely reported. In specific chiral hyperbolic metamaterial with a photonic Weyl system, the disorder-induced state transition was found recently in such photonic topological system [32]. We propose here the quantity T/T_0 to study the disorder properties in this work where T is the transmission detected along the finite red line at the exit of the straight interface and the subscript 0 means the nondisorder case, as seen in Fig. 8(a). From Figs. 5 and 7, two hexagons are sufficient to behave as bulk media to constrain the interface. To reduce the cost of finite element simulation, we employ a straight interface (in the blue dotted box) separated by two hexagon units in Fig. 8(a). Antisymmetric Lamb mode waves are excited at the finite white line. The whole structure is surrounded by PML.

Several types of disorder can be envisaged such as disorder in position, geometrical parameters (height, radius, contact, etc.), or physical parameters (density, elastic modulus). The

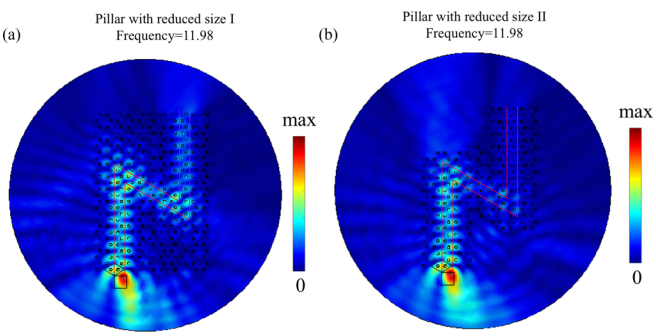

FIG. 7. Minimized bulk size with one hexagon unit on one side of the straight interface part (a) or on any side of the zigzag interface (b). The flexural wave source is excited at $\Omega a = 11.98$.

latter types will mainly affect the resonant frequency ω_R that will further change the Dirac frequency. Among those, the height h is one of the most interesting parameters for studying the resonant frequency. Therefore, we consider position and height of pillars for disorder study. For disorder in position, we allow pillar i at the interface to be randomly displaced $l_i = (x_i, y_i)$ with respect to its original position, as shown by the red dots in Fig. 8(b). The position disorder degree is defined as $100\% \max(|l_i|)/a$. For instance, in the example of Fig. 8(b) for 20% disorder degree in position, the moved displacement of pillar i in the interface is $-0.16a$ in the x axis and $0.1a$ in the y axis, corresponding to the red dot $l_i = (-0.16,\ 0.1)$. For disorder in height, we allow the height of pillar j at the interface to change by δh and the height disorder degree is defined as $100\% \max(\delta h)/h$. For instance, in the example of Fig. 8(c) for 25% disorder degree in height, the number j ($\delta h/h = -0.2$) means the height of pillar j is reduced by 20%.

Disorder is introduced either in the position or height of all the pillars at the interface and the random sampling is repeated at least five times at $\Omega a = 11.98$. The average T/T_0 (blue curve) as well as the root mean square of fluctuations (vertical red bars) are plotted in Fig. 9. For position disorder, one can observe that T/T_0 first remains stable for a small degree of disorder = (0%–5%), then decreases significantly with a linearlike trend against increasing position disorder degree. In Fig. 9(b), we show how the field of abs(u_z) changes at four different disorder degrees. Although T/T_0 decreases, the robustness of the topologically protected edge state abs(u_z) field is still conserved within large position disorder range (0, 20%) where T/T_0 is higher than 0.8. For height disorder, T/T_0 remains stable around 1 when the height disorder degree is not larger than 33%. Then it displays an abrupt drop within height disorder range of 40%–50% that behaves as a transition threshold. Figure 9(d) clearly shows how the edge state propagation is disturbed due to the effect of height disorder. From the last panels of Figs. 9(b) and 9(d), one can notice that the incident wave can hardly enter the interface from the bottom since the interface mode vanishes and most part of the wave is reflected towards the entrance, which results in low T/T_0 value.

IV. CONVENTIONAL INTERFACE STATES

An interface state can also be found for a zigzag type honeycomb lattice edge with different path shapes [15]. In this section, we present a way to design the edge state by band engineering with the displacement concentration formula (3). Let us consider a honeycomb unit cell with two cylindrical pillars of the same radius $R_c = 0.2a$ but different heights $h_A = 0.8a$ and $h_B = 0.4a$. The thickness of the plate is kept to $e = 0.1a$. Notice that comparing to the parameters in Sec. III, the radius increases and the height decreases, which contribute to increase the frequency of the pillar's bending and compressional resonances [33]; especially the blue shifted compressional resonance moves the potential Dirac point to a higher frequency range $\Omega a > 25$ beyond the first two resonant modes. In this section, the conventional edge state design does not depend on the Dirac point, but directly on the dispersion tailoring of a finite stripe.

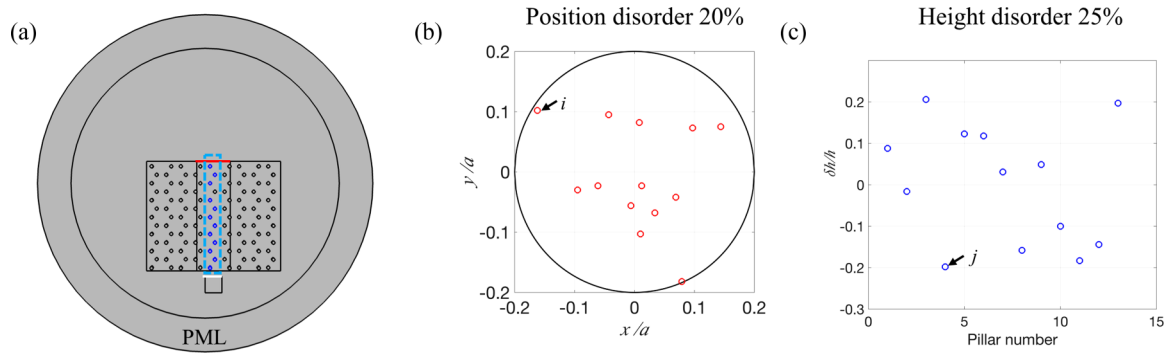

FIG. 8. (a) is the geometric model used in random simulation. The A_0 Lamb mode wave is excited by the finite white line source and the transmitted wave is detected by the finite red line. An example of position disorder 20% (b) and height disorder 25% (c) for all pillars in the interface (limited in the blue dotted box) is shown in (a); the dots in (b,c) show one example of the random profiles.

We first construct a finite stripe with one unit as shown in the lower part of Fig. 10(a). The stripe has a finite size along the y axis and Bloch-periodic boundary conditions are applied at the two edges along the x direction (the width is a along x). The dispersion is shown in Fig. 10(a) where the colors stand for the confinement of the modes in the four pillars contained in the two dotted boxes at the two edges in the y axis as compared to the whole strip. This localization is characterized by the parameter χ defined by

$$\chi = \frac{\iiint_{\text{box}} \sqrt{u_x^2 + u_y^2 + u_z^2}\, dV}{\iiint_{\text{stripe}} \sqrt{u_x^2 + u_y^2 + u_z^2}\, dV}. \tag{4}$$

Two bright and flat modes appear near the frequencies $\Omega a = 12$ and $\Omega a = 23$. The eigenmodes at $k_x a/\pi = 1$ of these two modes, labeled $k1$ and $k2$, are shown at the bottom in the left panel, revealing localized states of this finite stripe in one edge (pillar B at the left edge) and not at the other (pillar A at the right edge). We note that the $k1$ and $k2$ mode branches will disappear if the pillars at both left and right edges are chosen to be type A. Then we take the pillar B to design an interface as type A-B-B-A in the middle of a stripe, shown as the dotted rectangle at the bottom of Fig. 10(b). In the corresponding dispersion curve in Fig. 10(b), the color stands again for the concentration rate χ of the displacement in the four pillars at the interface (in the dotted box). Comparing Figs. 10(a) and 10(b), two new bands appear as localized interface modes in Fig. 10(b), where their eigenmodes labeled as $k11$ and $k22$ (shown in green color) are displayed. From the color bar maximum limit for the interface eigenmodes, the conventional interface states are more confined than the topologically protected design in Fig. 4. In Fig. 10(b), as the symmetric pillar at both the left and right edges of the stripe is pillar B, there are two degenerated localized states originating from the $k1$ and $k2$ modes of Fig. 10(a), namely, $k1a$ ($k2a$) and $k1b$ ($k2b$). If the symmetric pillars at both the left and right edges of the stripe in Fig. 10(b) were chosen to be pillar A, the branches associated to $k1a$, $k1b$ and $k2a$, $k2b$ disappear. From Figs. 10(a) and 10(b), one can identify the possible frequency domains where the interface modes can locate.

A zigzag A-B-B-A type interface with sharp corners is designed as in the previous section in order to compare the robustness of the interface states. The same pointlike flexural wave source is excited at the bottom of the interface at $\Omega a = 13.30$ and $\Omega a = 17.74$ in Figs. 11(a) and 11(b), respectively, showing the conventional interface mode works in a broadband frequency region. Nevertheless, we observe that the amplitude of the flexural wave propagation decreases when passing through the zigzag interface due to the backscattering effect at the sharp corners, while it almost remains uniform for the topologically protected edge state in Fig. 5. It is important to remark that the conventional edge mode is more "compact," in the sense that the evanescence of the wave into the surrounding bulk is faster.

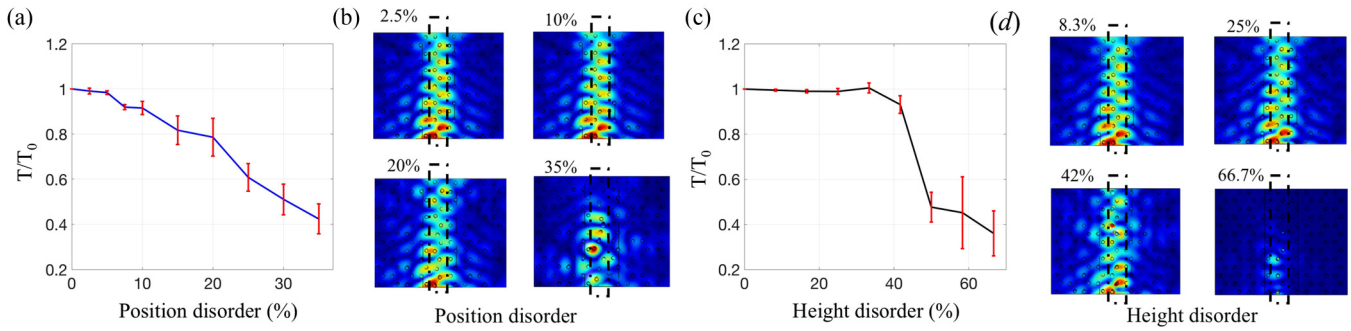

FIG. 9. (a) Relation between position disorder degree and T/T_0 at $\Omega a = 11.98$; (b) propagating states abs(u_z) at four values of position disorder. (c) Relation between height disorder degree and T/T_0 at $\Omega a = 11.98$; (d) propagating states abs(u_z) at four values of height disorder. The red vertical bars in (a,c) stand for the root mean square of fluctuations. Only the phononic crystal part (the circle surrounding the plate is not shown) of the whole geometry in Fig. 8(a) is shown in (b,c).

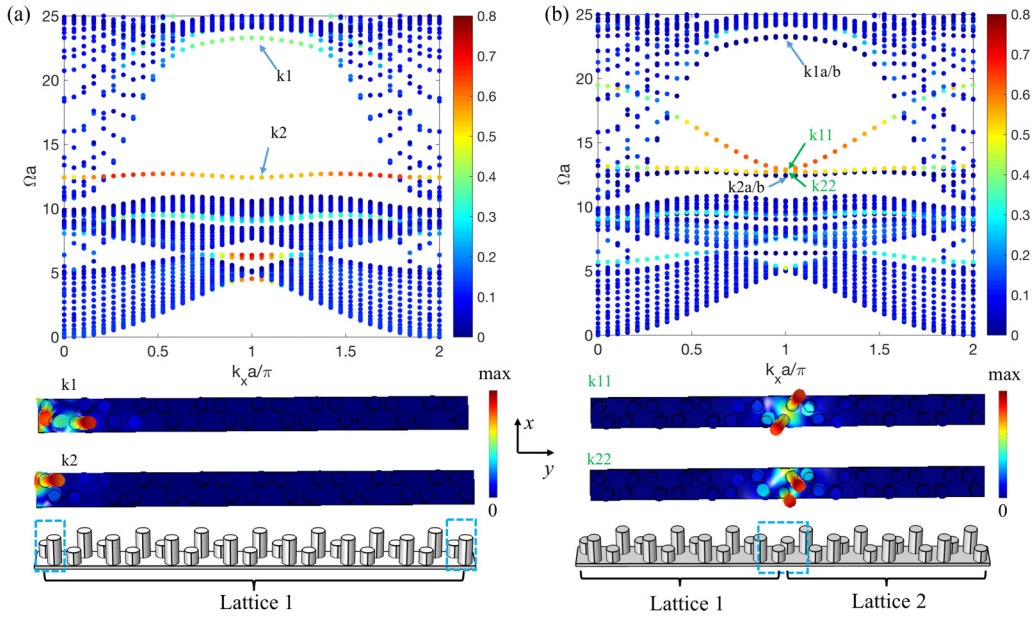

FIG. 10. (a) Dispersion of a stripe consisting of a unit cell with one honeycomb lattice as $h_A = 0.8a$ and $h_B = 0.4a$ where the color stands for the displacement concentration rate of the four pillars (in the two dotted boxes) at the two edges in y. The amplitudes of total displacement distributions at the $k1$ and $k2$ points shown at the bottom. (b) Dispersion of a stripe consisting of a unit cell with two lattices as an interface type $ABBA$ in the middle where the color stands for the displacement concentration rate of the four pillars (in the dotted box) at the middle interface. The amplitudes of total displacement distributions at the $k11$ and $k22$ points (green color) are shown at the bottom. Thickness of the plate $e = 0.1a$; radius of the pillar $r_p = 0.2a$.

To better understand the behavior of the interface states and the propagation along a zigzag path with defect and disorder, a $4a \times 4.3a$ model consisting of a B-B pillars interface in the dotted rectangle separated by one hexagon in the y direction is built and Bloch-periodic boundary conditions are applied to the edges in both the x and y directions, as shown in Fig. 11(c). The dispersion curves along the ΓX direction (square lattice of this supercell) are displayed in Fig. 11(d), with the color

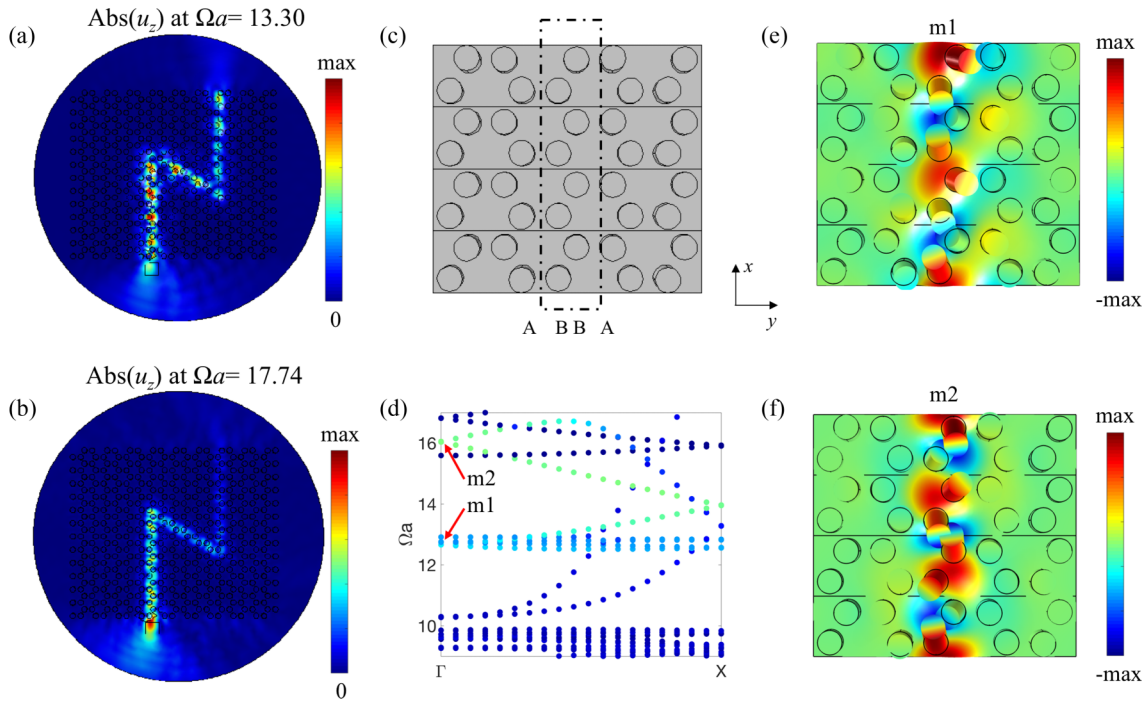

FIG. 11. Conventional interface states at $\Omega a = 13.30$ (a) and $\Omega a = 17.74$ (b,c) Geometry of a supercell model with two lattices as an A-B-B-A type interface (dotted rectangle) in the middle to better understand the conventional interface mode. The model has a size of $4a$ in x and $4.33a$ in y, with Bloch-periodic conditions applied to the edges in both directions The dispersion along $\Gamma \underline{X}$ is calculated and shown in (d) with two points at the Γ point as $m1$ and $m2$; the real parts of u_z of eigenmodes $m1$ and $m2$ points are shown in (e,f), respectively.

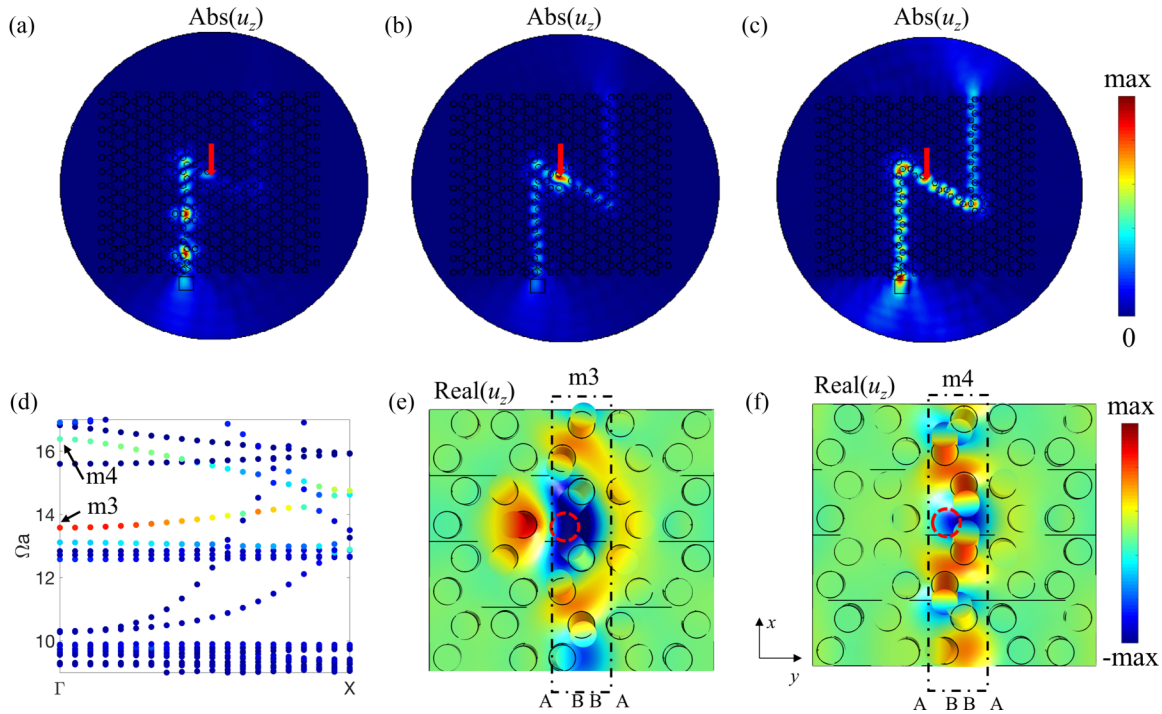

FIG. 12. Abs(u_z) of conventional interface states at $\Omega a = 13.30$ (a), $\Omega a = 13.75$ (b), and $\Omega a = 16.41$ (c) when moving a pillar in the central of the zigzag path indicated with a red arrow (the same as in the inset of Fig. 6); (d) dispersion along ΓX when moving one pillar in the interface, with the color standing for the displacement concentration rate on the two pillars in the neighborhood of the absent pillar position over the whole supercell; the real(u_z) of eigenmode $m3$ at $\Omega a = 13.75$ (e) and $m4$ at $\Omega a = 16.41$ (f) at the Γ point are shown, with the absent pillar indicated as the red dotted circle.

standing for the displacement concentration rate for eight pillars in the dotted rectangle over the whole model. It is clear that an interface mode (folded green bands) appears in the frequency range $\Omega a = [12.66,\ 16]$. The real part of u_z of the eigenmodes of points $m1$ and $m2$ at the Γ point are displayed in Figs. 11(e) and 11(f), respectively, showing a compact interface propagation.

In order to check the robustness of the propagation for the conventional edge state, a pillar at the same position in the zigzag path as in Fig. 6 is removed to see how the mode interacts with the defect. In Fig. 12, upper panel, simulations performed at $\Omega a = 13.30$ (a), $\Omega a = 13.75$ (b), and $\Omega a = 16.41$ (c) are presented as backscattered, defect localization, and propagation phenomena, respectively. We again calculate the dispersion curves of the $4a \times 4.3a$ model [Fig. 11(c)] but containing now the defect, namely, the removal of one pillar. The result along the ΓX direction is shown in Fig. 12(d) (the color stands for the displacement concentration rate on the two pillars in the neighborhood of the absent pillar position over the whole supercell in the dotted rectangle). We find that the

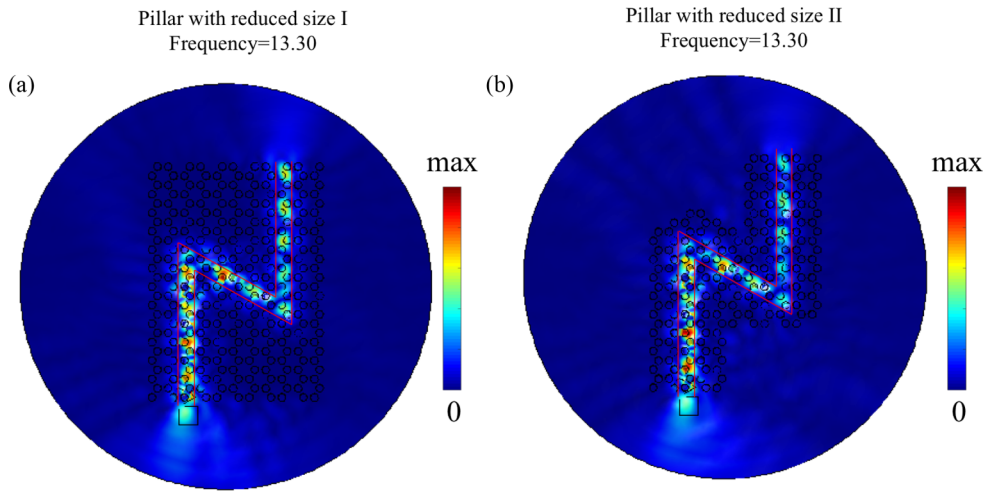

FIG. 13. Minimized bulk size with one hexagon unit on one side of the straight interface part (a) or on any side of the zigzag interface (b). Flexural wave source is excited at $\Omega a = 13.30$.

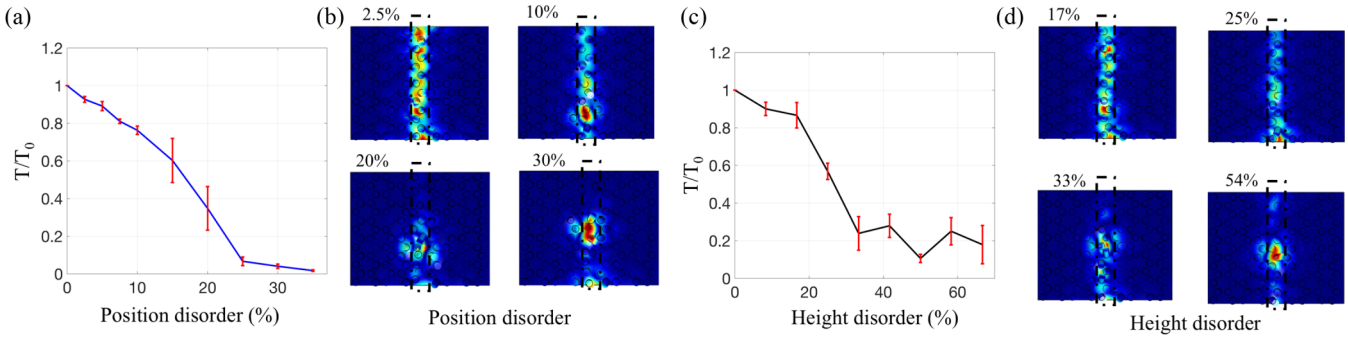

FIG. 14. (a) The relation between position disorder degree and T/T_0 at $\Omega a = 13.30$; (b) propagating states abs(u_z) at four position disorders; (c) the relation between height disorder degree and T/T_0 at $\Omega a = 13.30$; (d) propagating states abs(u_z) at four height disorders. The red vertical bars in (a,c) stand for the root mean square of fluctuations. Only the phononic crystal part of the whole geometry in Fig. 8(a) is shown in (b,c).

insertion of the defect will upward-shift the folded interface mode, starting now at $\Omega a = 13.75$ at the Γ point. The real(u_z) of eigenmode $m3$ at this $\Omega a = 13.75$ shown in (e) is symmetric along the y axis and behaves like a defect localized mode as in Ref. [34]. The eigenmode gradually changes from defect mode ($\Omega a = 13.75$) to a normal interface mode ($\Omega a = 16$). The real(u_z) of eigenmode $m4$ at frequency $\Omega a = 16$ shows wave propagation along the interface, seen in panel (f). Generally speaking, vibrating displacements are mostly concentrated in and/or around the defect area for a defect mode, while displacements are homogeneously distributed along the interface path for an interface mode. The up-shift defect-interface branch results in a very narrow band gap. The operating frequency $\Omega a = 13.30$ locates inside the narrow band gap while also being close to several flat localized modes, so that it is a partial propagating state in the lower straight waveguide of the zigzag path with backscattering effect. The narrow band gap, defect mode at $\Omega a = 13.75$, and interface propagating mode at $\Omega a = 16$ explain the different behaviors in (a)–(c), respectively. Meanwhile for the topologically protected interface mode, the propagation is protected against the defect as in Fig. 6.

Then we study the minimum size of the bulk phononic crystals surrounding the straight or zigzag interfaces to allow the interface state propagation. Unlike the minimized bulk phononic crystals' size behavior for topologically protected interface state in Fig. 7, we show in Fig. 13 that the conventional interface states are conserved for such a minimized surrounding of the interface, namely, one hexagon of bulk media surrounding the sharp corner. This result brings also *a posteriori* support to the validity of the reduced model introduced in Fig. 11(c), which was used for studying the propagation of the interface state in the zigzag path in the presence of defects and disorder. Indeed, in this model, the interface has exactly the same surroundings as in Fig. 13(b).

In Fig. 14, we study the similar disorder perturbations as in the last section for straight interface pillars that are separated by two hexagons in full wave simulations as in Fig. 8(a). For position disorder, T/T_0 decreases once the disorder is applied, and a linearlike trend is also found. When position disorder is larger than 25%, T/T_0 remains at very low values (weak transmitted wave). In Fig. 14(b), we can see the evolution of the interface propagation with different values of position disorder. For position disorder larger than 10%, waves are mainly trapped at specific locations in the interface path without penetrating into the bulk media, which can be explained by the dispersion analysis in Fig. 15 by taking the supercell in Fig. 11(c). In the upper panel of Fig. 15 for 10% position disorder, the dispersion of the supercell in Fig. 11(c) shows that the interface mode breaks with band gaps and waves are trapped in the interface. Similar results are found for 20% position disorder in the lower panel.

For height disorder, T/T_0 starts to slightly decrease until 17% height disorder, then it has a fast drop from 0.9 to about 0.25 within height disorder (17%, 33%), as a transition threshold, and finally keeps values around 0.25 for bigger height disorders, as seen in Fig. 14(c). From wave propagation distributions in Fig. 14(d), waves are mainly trapped at the interface with few parts exciting the upper interface boundary after the transition threshold (height disorder $\geqslant$33%). Therefore, a certain robustness of conventional edge state is exhibited for position disorder smaller than about 10% and height disorder smaller than about 17%.

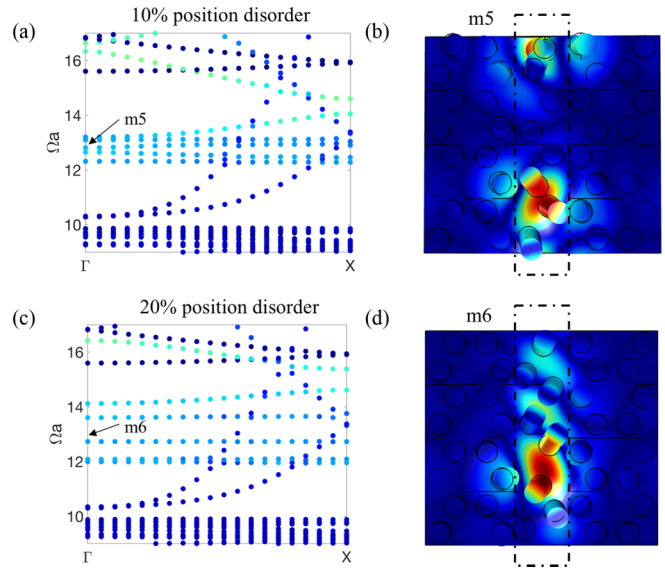

FIG. 15. (a) ΓX dispersion when 10% position disorder is applied to pillars in the dotted rectangle as in Fig. 11(c); (b) eigenmode abs(u_z) of $m5$ at the Γ point; (c) ΓX dispersion when there is 20% position disorder; (d) eigenmode abs(u_z) of $m6$ at the Γ point.

V. SUMMARY

This work analyzed the dispersion of both cylindrical and spherical resonators on a thin plate in a honeycomb lattice where we employed the known concept of breaking the inversion symmetry in the unit cell to obtain topologically protected edge states. These are found for both types of resonators, being more robust in the cylindrical case. We compared their properties with those of a conventional interface state without topological protection, which exhibits more confined propagation along a zigzag path. Due to the backscattering effect at the sharp corner of the path, the propagating wave's amplitude of the conventional edge state decreases when passing through the corners, unlike the topological states which are protected against backscattering. We also compared the behaviors of conventional and topologically protected interface states with the presence of defects. The topologically protected interface state is immune to the defect, while the conventional interface state changes to backscattered, defect localized, and propagating states resulting from the interaction between the defect and the interface mode. We also analyzed the required size of the bulk media to conserve the edge states, showing that conventional states require less bulk material than topologically protected states. Two typical physical disorder perturbations, namely, disorder in position and height, were applied also to all pillars in a straight interface, and the empirical parameter transmission ratio is employed to characterize the "transition threshold" of edge states under disorder perturbations. It was shown that in both designs the transmission ratio decreases quasilinearly against position disorder while it has an abrupt drop against height disorder, showing a kind of transition threshold. However, the ways in which edge states change after the transition threshold are different: An incident wave can hardly enter the interface for topological design, while the conventional edge state will become wave-trapped states in the interface. These comparisons help to understand, distinguish, and define conventional or topologically protected states, the understanding of which is more than relevant to properly develop the potential applications of these devices.

ACKNOWLEDGMENTS

Work supported by the US Office of Naval Research under Grant No. N00014-17-1-2445. Y.J. acknowledges a start-up fund from Tongji University. D.T. acknowledges financial support through the "Ramón y Cajal" fellowship.

[1] Y. Pennec, B. Djafari-Rouhani, H. Larabi, J. O. Vasseur, and A. C. Hladky-Hennion, Low-frequency gaps in a phononic crystal constituted of cylindrical dots deposited on a thin homogeneous plate, Phys. Rev. B **78**, 104105 (2008).

[2] T. T. Wu, Z. G. Huang, T. C. Tsai, and T. C. Wu, Evidence of complete band gap and resonances in a plate with periodic stubbed surface, Appl. Phys. Lett. **93**, 111902 (2008).

[3] Y. Jin, N. Fernez, Y. Pennec, B. Bonello, R. P. Moiseyenko, S. Hémon, Y. Pan, and B. Djafari-Rouhani, Tunable waveguide and cavity in a phononic crystal plate by controlling whispering-gallery modes in hollow pillars, Phys. Rev. B **93**, 054109 (2016).

[4] M. S. Kushwaha, P. Halevi, L. Dobrzynski, and B. Djafari-Rouhani, Acoustic Band Structure of Periodic Elastic Composites, Phys. Rev. Lett. **71**, 2022 (1993).

[5] M. M. Sigalas and E. N. Economou, Band structure of elastic waves in two dimensional systems, Solid State Commun. **86**, 141 (1993).

[6] M. I. Hussein, M. J. Leamy, and M. Ruzzene, Dynamics of phononic materials and structures: Historical origins, recent progress, and future outlook, Appl. Mech. Rev. **66**, 040802 (2014).

[7] Y. Pennec, J. O. Vasseur, B. Djafari-Rouhani, L. Dobrzynski, and P. A. Deymier, Two-dimensional phononic crystals: Examples and applications, Surf. Sci. Rep. **65**, 229 (2010).

[8] Y. Jin, Y. Pennec, Y. Pan, and B. Djafari-Rouhani, Phononic crystal plate with hollow pillars actively controlled by fluid filling, Crystals **6**, 64 (2016).

[9] Z. Liu, X. Zhang, Y. Mao, Y. Zhu, Z. Yang, C. T. Chan, and P. Sheng, Locally resonant sonic materials, Science **289**, 1734 (2000).

[10] G. Ma and P. Sheng, Acoustic metamaterials: From local resonances to broad horizons, Sci. Adv. **2**, e1501595 (2016).

[11] S. Cummer, J. Christensen, and A. Alù, Controlling sound with acoustic metamaterials, Nat. Rev. Mater. **1**, 16001 (2016).

[12] Y. Jin, Y. Pennec, Y. Pan, and B. Djafari-Rouhani, Phononic crystal plate with hollow pillars connected by thin bars, J. Phys. D: Appl. Phys. **50**, 035301 (2016).

[13] R. K. Pal and M. Ruzzene, Edge waves in plates with resonators: An elastic analogue of the quantum valley Hall effect, New J. Phys. **19**, 025001 (2017).

[14] R. Chaunsali, C. W. Chen, and J. Yang, Subwavelength and directional control of flexural waves in zone-folding induced topological plates, Phys. Rev. B **97**, 054307 (2018).

[15] D. Torrent, D. Mayou, and J. Sánchez-Dehesa, Elastic analog of graphene: Dirac cones and edge states for flexural waves in thin plates, Phys. Rev. B **87**, 115143 (2013).

[16] J. Vila, R. K. Pal, and M. Ruzzene, Observation of topological valley modes in an elastic hexagonal lattice, Phys. Rev. B **96**, 134307 (2017).

[17] J. Chen, S. Huo, Z. Geng, H. Huang, and X. Zhu, Topological valley transport of plate-mode waves in a homogenous thin plate with periodic stubbed surface, AIP Adv. **7**, 115215 (2017).

[18] T. W. Liu and F. Semperlotti, Tunable Acoustic Valley–Hall Edge States in Reconfigurable Phononic Elastic Waveguides, Phys. Rev. Appl. **9**, 014001 (2018).

[19] M. Z. Hasan and C. L. Kane, Colloquium: Topological insulators, Rev. Mod. Phys. **82**, 3045 (2010).

[20] P. Wang, L. Lu, and K. Bertoldi, Topological Phononic Crystals with One-Way Elastic Edge Waves, Phys. Rev. Lett. **115**, 104302 (2015).

[21] S. H. Mousavi, A. B. Khanikaev, and Z. Wang, Topologically protected elastic waves in phononic metamaterials, Nat. Commun. **6**, 8682 (2015).

[22] C. He, X. Ni, H. Ge, X. Sun, Y. Chen, M. Lu, X. Liu, L. Feng, and Y. Chen, Acoustic topological insulator and robust one-way sound transport, Nat. Phys. **12**, 1124 (2016).

[23] Z. Zhang, Q. Wei, Y. Cheng, T. Zhang, D. Wu, and X. Liu, Topological Creation of Acoustic Pseudospin Multipoles in a Flow-Free Symmetry-Broken Metamaterial Lattice, Phys. Rev. Lett. **118**, 084303 (2017).

[24] J. Lu, C. Qiu, L. Ye, X. Fan, M. Ke, F. Zhang, and Z. Liu, Observation of topological valley transport of sound in sonic crystals, Nat. Phys. **13**, 369 (2017).

[25] N. Boechler, J. K. Eliason, A. Kumar, A. A. Maznev, K. A. Nelson, and N. Fang, Interaction of a Contact Resonance of Microspheres with Surface Acoustic Waves, Phys. Rev. Lett. **111**, 036103 (2013).

[26] Y. Jin, E. B. El Houssaine, Y. Pennec, and B. Djafari-Rouhani, Tunable Fano resonances of Lamb modes in a pillared metasurface, J. Phys. D: Appl. Phys. **50**, 425304 (2017).

[27] S. Bittner, B. Dietz, M. Miski-Oglu, P. O. Iriarte, A. Richter, and F. Schaefer, Observation of a Dirac point in microwave experiments with a photonic crystal modeling graphene, Phys. Rev. B **82**, 014301 (2010).

[28] W. Zhong and X. Zhang, Dirac-cone photonic surface states in three-dimensional photonic crystal slab, Opt. Express **19**, 13738 (2011).

[29] X. Zhang and Z. Liu, Extremal Transmission and Beating Effect of Acoustic Waves in Two-Dimensional Sonic Crystals, Phys. Rev. Lett. **101**, 264303 (2008).

[30] D. Torrent and J. Sánchez-Dehesa, Acoustic Analogue of Graphene: Observation of Dirac cones in Acoustic Surface Waves, Phys. Rev. Lett. **108**, 174301 (2012).

[31] Y. Jin, D. Torrent, and B. Djafari-Rouhani, Invisible omnidirectional lens for flexural waves in thin elastic plates, J. Phys. D: Appl. Phys. **50**, 225301 (2017).

[32] C. Liu, W. Gao, B. Yang, and S. Zhang, Disorder-Induced Topological State Transition in Photonic Metamaterials, Phys. Rev. Lett. **119**, 183901 (2017).

[33] Y. Jin, B. Bonello, R. P. Moiseyenko, Y. Pennec, O. Boyko, and B. Djafari-Rouhani, Pillar-type acoustic metasurface. Phys. Rev. B **96**, 104311 (2017).

[34] R. Marchal, O. Boyko, B. Bonello, J. Zhao, L. Belliard, M. Oudich, Y. Pennec, and B. Djafari-Rouhani, Dynamics of confined cavity modes in a phononic crystal slab investigated by *in situ* time-resolved experiments, Phys. Rev. B **86**, 224302 (2012).